ANNALS OF THE NEW YORK ACADEMY OF SCIENCES
Issue: *Tight Junctions and their Proteins*
ORIGINAL ARTICLE

A cCPE-based xenon biosensor for magnetic resonance imaging of claudin-expressing cells

Anna Piontek,[1,a] Christopher Witte,[2,a] Honor May Rose,[2] Miriam Eichner,[3] Jonas Protze,[1] Gerd Krause,[1] Jörg Piontek,[3,b] and Leif Schröder[2,b]

[1]Leibniz-Forschungsinstitut für Molekulare Pharmakologie (FMP), Structural Bioinformatics and Protein Design, Berlin, Germany. [2]Leibniz-Institut für Molekulare Pharmakologie (FMP), Molecular Imaging, Berlin, Germany. [3]Institute of Clinical Physiology Charité – Universitätsmedizin Berlin, Berlin, Germany

Address for correspondence: Gerd Krause, Leibniz-Institut für Molekulare Pharmakologie (FMP), Structural Biology, Robert Roessle Str. 10, Berlin 13125, Germany. GKRAUSE@fmp-berlin.de

The majority of malignant tumors originate from epithelial cells, and many of them are characterized by an overexpression of claudins (Cldns) and their mislocalization out of tight junctions. We utilized the C-terminal claudin-binding domain of *Clostridium perfringens* enterotoxin (cCPE), with its high affinity to specific members of the claudin family, as the targeting unit for a claudin-sensitive cancer biosensor. To overcome the poor sensitivity of conventional relaxivity-based magnetic resonance imaging (MRI) contrast agents, we utilized the superior sensitivity of xenon Hyper-CEST biosensors. We labeled cCPE for both xenon MRI and fluorescence detection. As one readout module, we employed a cryptophane (CrA) monoacid and, as the second, a fluorescein molecule. Both were conjugated separately to a biotin molecule via a polyethyleneglycol chemical spacer and later via avidin linked to GST–cCPE. Nontransfected HEK293 cells and HEK293 cells stably expressing Cldn4–FLAG were incubated with the cCPE-based biosensor. Fluorescence-based flow cytometry and xenon MRI demonstrated binding of the biosensor specifically to Cldn4-expressing cells. This study provides proof of concept for the use of cCPE as a carrier for diagnostic contrast agents, a novel approach for potential detection of Cldn3/-4–overexpressing tumors for noninvasive early cancer detection.

Keywords: *Clostridium perfringens* enterotoxin; claudin; tumor; molecular resonance imaging; xenon; Hyper-CEST

Introduction

The claudin (Cldn) protein family contains at least 27 members in mammals. These tetraspan transmembrane proteins are the main constituent of tight junctions (TJs), which are essential to maintain epithelial cell polarity and regulate paracellular permeability.[1] Their upregulation has been discussed as a potential marker in oncology. The majority of malignant tumors originate from epithelial cells. Though some carcinomas originating from different tissues are characterized by low claudin expression,[2] most ovarian, gastric, hepatic, breast, colon, pancreas, and other tumors of epithelial origin show upregulated Cldn3 and -4 expression.[2–14] In addition to such aberrant expression, the localization of claudin proteins outside of TJs may contribute to their role in tumorigenesis, since claudin mislocalization can impede barrier function and alter claudin-mediated signaling.[3] Claudins that are overexpressed in tumors do not necessarily contribute to TJ sealing and paracellular barrier function. For instance, in human colorectal tumors, Cldn1, -3, and -4 are upregulated, but TJs are disorganized.[4] Delocalization of Cldn1 and -4 from TJs in bladder tumors[5] and the effects of altered localization of Cldn7 on the invasiveness of esophageal carcinoma[6] have been reported. It has also been assumed that increased expression of claudins may promote tumor progression through positive effects on cell migration, invasion, and metastasis.[2,15]

[a]These authors share first authorship.
[b]These authors share last authorship.

doi: 10.1111/nyas.13363

Thus, to improve diagnosis or treatment of cancers of epithelial origin, claudins, such as Cldn4, are promising targets owing to their tumor specificity and high accessibility caused by overexpression and mislocalization (outside of TJs) in the cell membrane.

The *Clostridium perfringens* enterotoxin (CPE) has a unique claudin-binding profile and has shown great potential to act as a targeting unit as part of a noninvasive tool for early cancer detection. CPE interacts with a very specific subset of the claudin family. It binds with high affinity (K_d ~10 nM) to Cldn3, -4, -6, -7, and -9; with medium affinity to Cldn8, -14, and -19; with low affinity to Cldn1 and -2; but does not bind to Cldn5, -10 to -13, -15 to -18, and -20 to -24.[7,8] CPE is released by *C. perfringens*-type A strains and causes food poisoning. It is a β-pore–forming toxin that is cytotoxic to epithelial cells. In contrast, the C-terminal domain of CPE (amino acids 194–319 (cCPE)) alone has been shown to be devoid of toxicity *in vitro*[9] and *in vivo*[10] but preserves binding activity to the receptors (claudins).[11,12]

cCPE coupled to infrared fluorophores was used for optical detection of pancreatic cancer in mice.[13] Therefore, the use of cCPE-based biosensors is a novel diagnostic approach for *in vivo* detection of Cldn3/-4–overexpressing tumors.[14] However, fluorescence-based imaging is limited *in vivo* by penetration depth and autofluorescence. In comparison, magnetic resonance imaging (MRI) contrast agents overcome these limitations with an effectively unlimited penetration depth. Though MRI provides exquisite anatomical images, particularly for soft tissue, it currently lags behind other molecular imaging modalities owing to its poor sensitivity. Translating knowledge about molecular targets into MRI reporters remains a challenge for conventional, relaxivity-based contrast agents. Protein-targeted relaxivity agents based on gadolinium (Gd) chelates have been developed, but even those compounds with high relaxivity require micromolar Gd concentrations,[15] which exceeds the abundance of many targets of interest.

Next-generation MRI biosensors, such as the xenon Hyper-CEST biosensor, have MRI detection limits down to the picomolar range[16–18] and are greatly expanding the scope of possible targets that can be addressed using MRI. Though still in the early stages of development, xenon biosensors have the potential to radically improve molecular imaging using MRI.[19] Such biosensors achieve this high sensitivity utilizing three key elements.

Spin-hyperpolarization

Spin-hyperpolarization of xenon, through spin exchange optical pumping (SEOP),[20] increases xenon's detectable MRI signal by 4–5 orders of magnitude. Modern SEOP hyperpolarizers can produce xenon with polarizations as high as 25% in continuous flow[21] and reach 100% in batch mode.[22] With such high polarizations, the vast majority of xenon nuclei contribute to the detected signal, rather than the insignificant fraction that contributes under normal conditions (~0.001% at fields of 9.4 T). In addition to being essential for the development of xenon biosensors, hyperpolarization has already led to the successful use of xenon MRI, delivered either by inhalation or injection, for imaging of void spaces in the human lung[23] and highly perfused organs, such as the rodent[24,25] and human brain.[26]

Advanced xenon contrast agents

Advanced xenon contrast agents, through large changes in chemical shift, allow bound xenon to be distinguished from unbound xenon in both spectroscopy and imaging. Such agents produce switchable contrast and can be multiplexed, allowing the simultaneous readout of multiple specific biomarkers. Typically, this is achieved using a xenon molecular host, such as CrA, which can transiently and reversibly bind a single xenon atom and act as a xenon contrast agent.[27] Though cryptophanes are the most commonly used host for xenon biosensors, alternative molecular hosts, such as cucucurbiturils[28] and nanoemulsions[29] as well as genetically encoded gas vesicles,[30] have also been successfully used. Importantly, the binding between xenon and such hosts occurs spontaneously, even in complicated biological environments.[16] This allows the targeted contrast agent to be delivered hours to days before the xenon is administered (in the high field of the magnet immediately before imaging), allowing plenty of time for its accumulation at the site of interest and wash out elsewhere (though perfect timing of delivery will likely need to be optimized for different biosensors owing to differences in degradation rates and pharmacokinetics). This is of particular importance owing to the finite lifetime of hyperpolarization and presents a major advantage when compared with other

hyperpolarized reporters, such as ^{13}C-labeled pyruvate. Together, this enables xenon Hyper-CEST biosensors to seriously address the sensitivity problem of MRI.

Optimized detection using Hyper-CEST

Chemical exchange saturation transfer (CEST) is currently being investigated in a whole new class of MRI contrast agents to expand the range of diagnostic parameters, including oncology-related aspects, such as tumor pH[31–33] or enzymatic activity.[34,35] The CEST sensitivity enhancement relies on using a few reporter molecules to manipulate the magnetization of many exchanging labile protons in diamagnetic substances (diaCEST) or of many water molecules that are temporarily associated with or in close proximity to paramagnetic lanthanide chelates (paraCEST agents[36] and their inclusion into liposomes[37] or into red blood cells[38,39]). Hyper-CEST[40] combines hyperpolarization with CEST to further improve the sensitivity down to nano- to picomolar concentrations of the biosensors. It is an indirect detection method that relies on the constant exchange of xenon in and out of a host structure, such as CrA.[40] This ensures that each targeted host structure affects the magnetization of hundreds to thousands of xenon atoms.

Xenon biosensors were originally devised as responsive MRI contrast agents because their resonance frequency can change upon interaction with the target.[41] Since observation of this effect in cellular environments is challenging, some studies investigated their specificity when coupling the xenon host to highly efficient binding units. Recently, we presented the design of a flexible and modular platform for xenon biosensors on the basis of antibody targeting.[42] This design uses the high-affinity binding partners avidin and biotin to connect two functional modules, a targeting module and a readout module. These modules can be changed at will for different applications. In this initial study, the biosensor was targeted to CD14, a well-characterized macrophage marker, to localize target cells using xenon MRI.

Here, we developed a xenon Hyper-CEST biosensor for Cldn3/4 using this modular platform. Not only does this demonstrate the flexibility of this xenon biosensor platform by extending it beyond antibody targeting, but it also presents one possible pathway for translating the detection of Cldn3/4 to an MRI diagnostic tool with superior sensitivity compared with relaxivity contrast agents.

Materials and methods

Plasmids

For construction of plasmid encoding the GST–CPE194–319 (GST-cCPE) fusion protein, cDNA of CPE (kindly provided by Dr. Y. Horiguchi, Osaka University, Osaka, Japan) was amplified by polymerase chain reaction and cloned into pGEX-4T1 (GE Healthcare, Munich, Germany) using EcoRI and SalI.[43] A plasmid encoding GST–CPE194–319 with the single mutation K257A was generated by site-directed mutagenesis of pGEX–4T1–CPE194–319.[44]

The plasmid pCMV10/huCldn4 for expression of human Cldn4 with N-terminal FLAG was kindly provided by Dr. Susanne Milatz, Institute of Physiology, Kiel, Germany.

Expression and purification of cCPE constructs

CPE194–319-K257A with an N-terminal GST fusion was expressed in *Escherichia coli* BL21 strain. Bacteria were grown to A600 = 0.6–0.8, expression was induced by addition of 1 mM isopropyl-β-D-thiogalactopyranosid, and 3 h later bacteria were harvested (10 min, 20,000 × *g*, 4 °C), lysed in PBS with 1% (v/v) Triton X-100, 0.1 mM PMSF, 1 mM EDTA, protease inhibitor cocktail (Sigma–Aldrich, Darmstadt, Germany), and sonicated with Vibra CellTM Model 72434 (BioBlock Scientific, Illkirch, France) by 10 × 1-s pulses. To remove insoluble cell debris, lysates were centrifuged at 20,000 × *g* for 1 h at 4 °C. The proteins were purified from supernatants using glutathione–agarose (Sigma–Aldrich), and eluted proteins were dialysed against HEPES buffer, pH 8.2. Protein concentration was determined with BCA Protein Kit (Thermo Scientific, Rockford, IL).

Cell culture and transfection

HEK293 cells (HEK cells) were maintained in Dulbecco's modified Eagle's medium supplemented with 10% fetal calf serum, 100 units/mL penicillin, and 100 μg/mL streptomycin and were grown at 37 °C in a humidified incubator with 5% CO_2. Transfection of HEK cells with human Cldn4–FLAG was performed with Lipofectamine 2000 (Invitrogen, Waltham, MA). Stable clonal lines were

generated by selection with 500 μg/mL geneticin (G418, PAA Laboratories, Germany).

Synthesis of the biotinylated cryptophane-A (CrA) module

The CrA–biotin module was synthesized as described previously[42] using microwave (mw)-assisted acylation to connect CrA monoacid (provided by Kangyuan Jiyi, Inc., Shangdong, China) with biotin–PEG3–amine (ChemPrep), with a final yield of 48%. The construct was purified via reversed-phase high-performance liquid chromatography with a UV/Vis detector (RP-HPLC/UV), and its mass confirmed using an AB SCIEX 5800 MALDI TOF mass spectrometer (Applied Biosystems, Forster City, CA). Stock solution of the biotin conjugate was made in dimethyl sulfoxide (DMSO).

Avidin–cCPE biosensor conjugates

One milligram of GST–cCPE-K257A (molecular mass 41 kDa) protein was conjugated with avidin (molecular mass 67 kDa) using the commercially available Avidin Conjugation Kit 1 mg (Abcam, Cambridge, UK) according to manufacturer's instructions to yield avidin–protein conjugates. The estimated conjugation ratio of GST–cCPE-K257A to avidin was 1:1 and resulted in a construct with molecular mass 108 kDa. The complete biosensor conjugate was prepared *in vitro* by incubation of 1 mg avidin–GST–cCPE-K257A conjugate with a 40-fold molar excess of CrA–biotin conjugates (readout modules) in a mole ratio of 1: 3 fluorescein–biotin (Thermo Scientific) to CrA–biotin for 30 min in the dark at room temperature. After incubation, the product was purified and concentrated fivefold through an Amicon Ultra 15, 100-kDa concentrator (Merck Millipore, Darmstadt, Germany). This separated the fully labeled protein conjugates (molecular mass 113 kDa) from any unbound biotin conjugates (CrA–biotin, 1339.54 Da and fluorescein–biotin, 732.80 Da) in the product. The final CrA–fluorescein protein conjugates were concentrated to 0.25 mg/mL (2.21 μM) in PBS 1% DMSO and stored at 4 °C.

Incubation of cells with biosensors

For xenon MRI experiments, the adherent cells were incubated for 30 min in the dark at 37 °C with labeled GST–cCPE (18 μg/mL (160 nM) CrA–fluorescein protein conjugates) in 10 mL of serum-free medium, washed under light protection with serum-free media, harvested, pelleted by centrifugation (1200 rpm for 5 min at 4 °C), and resuspended in 2 mL of ice-cold PBS (Biochrom AG, Berlin, Germany). A 10-μL sample was taken for cell counting and viability analysis with Trypan Blue 0.5% (Biochrom AG) using a TC20 Automated Cell Counter (Bio-Rad, Munich, Germany). All cells used in further experiments had >95% viability as assessed by Trypan Blue analysis. Next, 5×10^6 cells/mL of non- and Cldn4–FLAG–transfected cells after incubation with Cldn4 biosensor were adjusted to a volume of 1 mL with ice-cold PBS. Then, 0.5 mL (2.5×10^6 cells) of the Cldn4–FLAG–transfected cells and 0.7 mL (3.5×10^6 cells) of non-transfected cells in suspension were used for xenon MRI, and 0.5×10^6 of each cell type in 0.1 mL of the suspension were used for flow cytometry.

Immunostaining and laser-scanning microscopy

HEK cells were seeded 40% confluent on poly-L-lysine (Sigma–Aldrich)–coated glass cover slips in 24-well plates. On the next day, confluent cell monolayers were incubated for 30 min at 37 °C with assembled Cldn4 biosensor dissolved in serum-free medium at a final concentration of 160 nM. After twice washing with PBS, cells were fixed with 3.7% paraformaldehyde (Sigma–Aldrich); blocked 10 min in PBS, 1% BSA, 0.02% Tween; and immunostained with rabbit anti-FLAG antibody (Invitrogen) for 1 h, followed by incubation with mouse anti-GST antibody (Sigma–Aldrich) for 1 h, incubation with mixture of AlexaFluor®594- or 647-conjugated goat anti-rabbit and AlexaFluor 488-conjugated goat anti-mouse secondary antibody (Invitrogen); and 10 min DAPI staining for nuclei visualization.

HEK Cldn3–YFP[45] and HEK Cldn4–FLAG were washed with PBS, fixed with methanol at –20 °C for 10 min; washed three times with PBS; blocked for 10 min in PBS, 1% BSA, 0.02% Tween; and immunostained with mouse anti-Cldn4 antibody (Invitrogen) for 1 h, followed by incubation with goat anti-mouse AlexaFluor 594 for 30 min and DAPI for 5 minute.

Fluorescent signals of fluorescein, secondary antibodies, and DAPI were identified by confocal microscopy (Zeiss LSM 780, Carl Zeiss Jena GmbH, Jena, Germany).

Flow cytometry

For flow cytometry (Figs. 2 and 3E and F), 0.5×10^6 cells were removed from samples after incubation with assembled biosensor as described above. Cell samples of nontransfected and Cldn4–FLAG–transfected HEK cells were resuspended in 500 μL of ice-cold PBS and kept in the dark, on ice, before the flow cytometry measurement. The absolute fluorescence intensity of fluorescein was measured and compared for each cell line under identical acquisition parameters. Flow cytometry was performed on a BD FACSCalibur flow cytometer using BD CellQuest Pro Acquisition software (BD Biosciences, San Jose, CA). Data were analyzed with FlowJo (FlowJo, LLC, Ashland, OR) analysis software. The mean of the median absolute fluorescence from triplicate experiments is shown as a diagram.

Hyper-CEST experiments

After incubation with the biosensor (as described above), the cells were resuspended at a concentration of 5×10^6 cells/mL in PBS. To reduce foam formation when bubbling the xenon gas mix, 0.2% of Pluronic L-81 (BASF) was added just before MRI measurements. The cell suspension was transferred to a nuclear magnetic resonance (NMR) two-compartment bubbling chamber (Fig. 2), with the Cldn4–FLAG–transfected HEK cell suspension in the inner compartment and the nontransfected HEK cells in the outer compartment. This setup was then connected to the hyperpolarized xenon MRI system and placed inside the magnet.

Hyper-CEST spectroscopy and imaging

All MRI studies were performed using a 9.4-T Bruker AV 400 wide-bore NMR spectrometer (Bruker Biospin, Ettlingen, Germany) fitted with gradient coils for imaging. A 10-mm inner-diameter double-resonant (^{129}Xe and ^{1}H) probe was used for excitation and detection. A custom-designed continuous-flow polarizer was used to produce hyperpolarized xenon by spin-exchange optical pumping.[21,46] A gas mixture of 5% xenon (26.4% ^{129}Xe natural abundance), 10% N_2, and 85% He was used. The hyperpolarized xenon gas mix was directly bubbled into the phantom containing the samples by using a spectrometer-triggered bubble dispenser (3.5-bar overpressure) via fused silica capillaries (Polymicro Technologies, Molex Incorporated, Caudebec lès Elbeuf, France). The bubbling was triggered by using spectrometer-triggered gas-flow regulators (mass flow controllers, Omega Newport, Deckenpfronn, Germany).

For the Hyper-CEST image of the cells incubated with the biosensor, 10 on-resonant and 10 off-resonant scans were taken and averaged. For each image, the xenon gas mix was bubbled into solution for 15 s followed by a 3-s delay to allow bubbles to collapse. This was followed by a 20-s, 30-μT saturation pulse (–124 ppm for the on-resonant scan and 124 ppm for the off-resonant scan). The image was read out using a Rapid Acquisition with Relaxation Enhancement (RARE)[47] readout (slice thickness, 20 mm; matrix size, 32×32; in-plane resolution, 625 μm; linear k-space encoding; bandwidth, 8 kHz; echo time, 7 ms; acquisition time, 168 ms; and RARE factor, 32). For the Hyper-CEST spectrum, 20 images were acquired with the same RARE readout after saturating at different frequencies (each saturation pulse was for 20 s with a power of 30 μT). With regard to the choice of linear over centric encoding, we have found that the encoding only has a marginal effect on the CEST contrast, as the saturation pulse that generates this contrast is a preparatory step. In addition, we found that the linear encoding gave fewer artifacts in the image (i.e., centric encoding leads to a blurring in the phase direction). Image processing (Figs. S1 and S2) was performed using Python (Python Software Foundation, http://www.python.org).

Results

Preparation of a cCPE-based biosensor for MR molecular imaging of Cldn3- and Cldn4-expressing cells

This study aimed to generate a cCPE-based xenon Hyper-CEST biosensor to detect Cldn3 or -4 by MR molecular imaging. The experimental design is depicted in Figure 2. For coupling the MRI readout module to the cCPE-based targeting module (Fig. 2, top), the latter had to be conjugated to avidin on an accessible lysine residue on the surface of cCPE. Using the cCPE crystal structure (PBD ID: 2QUO[48]), seven suitable lysines were identified enabling efficient amino group–directed conjugation of avidin. However, identification of the cCPE–Cldn3/-4 binding interfaces revealed that K257 of cCPE is oriented close to the binding pocket for the extracellular loop 2 of claudins (red circle in Fig. 1A).[43,44] A bulky readout module coupled to K257 probably disturbs claudin binding. Therefore,

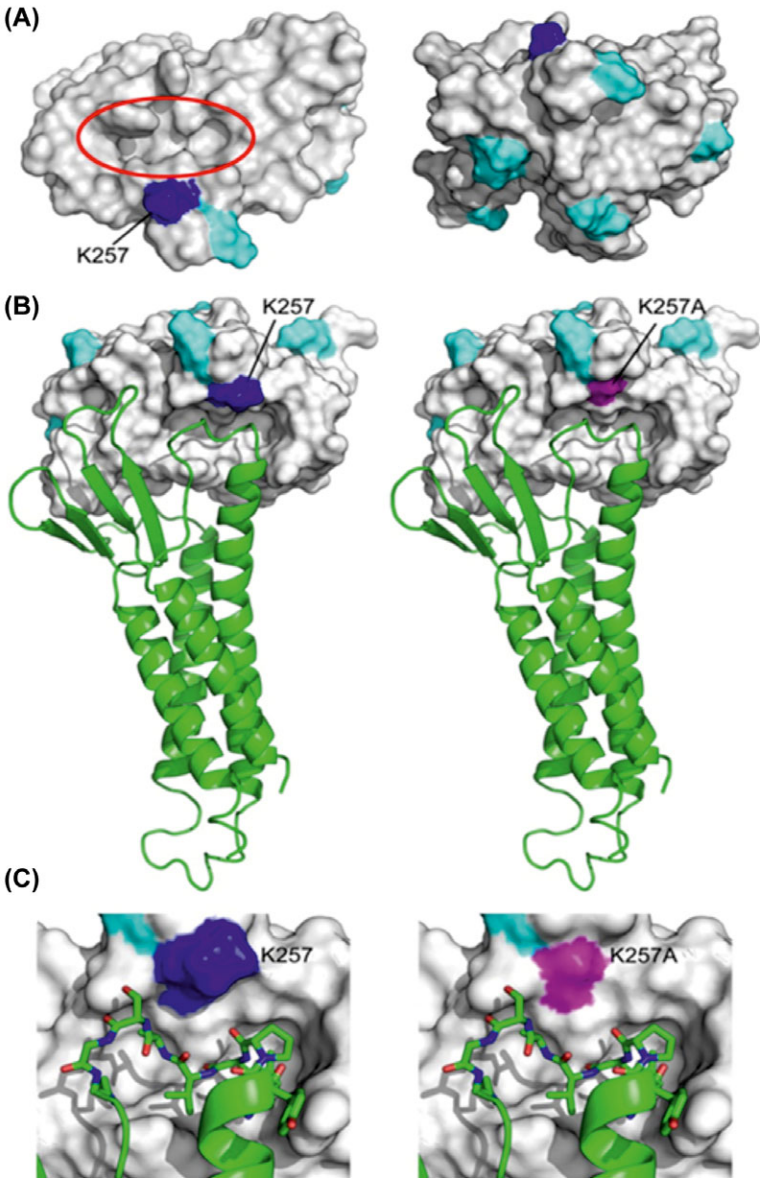

Figure 1. Homology model of cCPE-K257A bound to Cldn4. (A) cCPE (PDB ID: 2QUO[48]) top (left) and side view (right) shown as surface. Available lysines highlighted in cyan and K257 highlighted in blue. Binding pocket for ECL2 of claudin indicated by red circle. (B) Left: Crystal structure of cCPE (PDB ID: 5B2G,[66] surface, K257 blue) with Cldn4 (cartoon, green). Right: model of cCPE-K257A (surface, K257A magenta) with Cldn4 (cartoon, green). (C) Close-up of B with the residues of the cCPE-binding motif NPLVASGQ in the ECL2 of Cldn4 depicted as sticks (C, green; O, red; and N, blue). K257 does not interact with the ECL2 of Cldn4. A bulky readout module conjugated to K257 probably causes steric hindrance. This can be prevented by substitution to alanine, which does not alter the shape of the claudin-binding pocket drastically.

we substituted K257 with alanine. Binding studies showed that the cCPE-K257A mutant was still able to bind efficiently to Cldn3 and -4.[44] Since this cCPE mutant (Fig. 1) prevents potential blocking of claudin-binding by steric hindrance of a coupled readout module to K257, it was selected for further biosensor generation. GST–cCPE-K257A was expressed in *E. coli* and purified, and avidin was

conjugated via an amino group–reactive linker. The GST tag also possesses, on its surface, 12 lysine residues that can potentially be coupled to avidin and increase the number of readout units per targeting unit. This avidin–cCPE targeting module was linked to biotin–fluorescein and biotin–CrA as readout modules to obtain the biosensor, hereafter referred to as the Cldn4 biosensor.

Detection of Cldn4-expressing cells via the cCPE-based biosensor

First, we tested whether the Cldn4 biosensor was able to label Cldn4-expressing cells specifically. For this, we generated HEK cell line stably expressing FLAG-tagged human Cldn4. Expression of Cldn4–FLAG was verified by immunostaining (Fig. 3A and B). Next, the claudin-free parental HEK cell line was compared with the HEK line stably expressing Cldn4–FLAG. Living cells were incubated with 160 nM of the Cldn4 biosensor for 30 min at 37 °C, washed to remove unbound biosensor, and harvested (Fig. 2, step 2).

Binding was first analyzed by confocal microscopy. In contrast to the nontransfected HEK cells, the biosensor was detected via fluorescein fluorescence and GST anti-immunoreactivity for Cldn4–FLAG–expressing HEK cells (Fig. 3C and D). In addition, binding of the biosensor to the cells was analyzed by means of flow cytometry and quantification of the fluorescein fluorescence (Fig. 3E and F). For Cldn4-expressing HEK cells, the fluorescein fluorescence was 48 times higher than for nontransfected HEK cells (Fig. 3E). This result shows that the Cldn4 biosensor specifically binds to cells in a Cldn4-dependent manner.

Hyper-CEST MRI detection of Cldn4-expressing cells

Next, we tested the ability of the Cldn4 biosensor to distinguish the target cell line (HEK expressing Cldn4–FLAG) from control cells (nontransfected HEK) by xenon Hyper-CEST MRI. The Cldn4-expressing and nonexpressing HEK cells were separately incubated with the Cldn4 biosensor, harvested, and placed in separate compartments within the MRI phantom (Fig. 2, step 4), which serves as a sample container that defines two volumes with different cellular environments. A false-color Hyper-CEST image overlaid a high-resolution proton image for reference (Fig. 4A and Supplementary online Figs. S1 and S2), which clearly identified the compartment with target cells and therefore confirmed that the Cldn4 biosensor can distinguish between cells with and without Cldn4. A quantitative evaluation of the ability of this technique for discriminating between these two cells lines is shown in Figure 4B. Plotting a histogram of the Hyper-CEST effect measured in each of the compartments, even in the presence of some unspecific binding, two distinct populations with very little overlap (outer compartment: median of 11% CEST effect, inner compartment: median of 59% CEST effect) were observed. In Figure 4C, a Hyper-CEST spectrum from each of the compartments is plotted. The unique spectral signature of xenon bound to host CrA in a lipidic/cellular environment (a resonance at ∼–120 ppm from the resonance from xenon free in solution[16,39]) is observed in both compartments (thereby giving evidence that the molecular environment is the same) but most strongly in the inner compartment.

Discussion

Targeting claudins that are overexpressed and localized outside of TJs on the surface of tumor cells of epithelial origin has considerable potential as a novel and noninvasive method for early cancer detection. For example, Cldn4 is expressed at high levels in the majority of epithelial ovarian tumors, irrespective of subtype, and is associated with tumor cells that are both chemoresistant and highly mobile. Ovarian cancer remains the most lethal gynecologic malignancy in the United States,[49] and delayed diagnosis could play a crucial role. Thus, owing to lack of effective screening programs, two-thirds of the patients with ovarian cancers are diagnosed with late stage (III–IV) cancer, and 90% of them develop later chemotherapy-resistant tumors and thereby succumb to their disease.[50] Though surgery is one of the most common treatment methods of ovarian cancer, and optimal tumor removal at the time of surgery is a crucial prognostic factor, the identification of micrometastatic disease remains extremely challenging.[51]

Given this, it is no surprise that different fluorescence-based biosensors have been developed for targeted claudin imaging.[13,51] For instance, Neesse and colleagues used cCPE coupled to the cyanine dye Cy5.5, 2D planar fluorescence reflectance imaging technology, and 3D fluorescence-mediated tomography for detection of pancreatic tumor

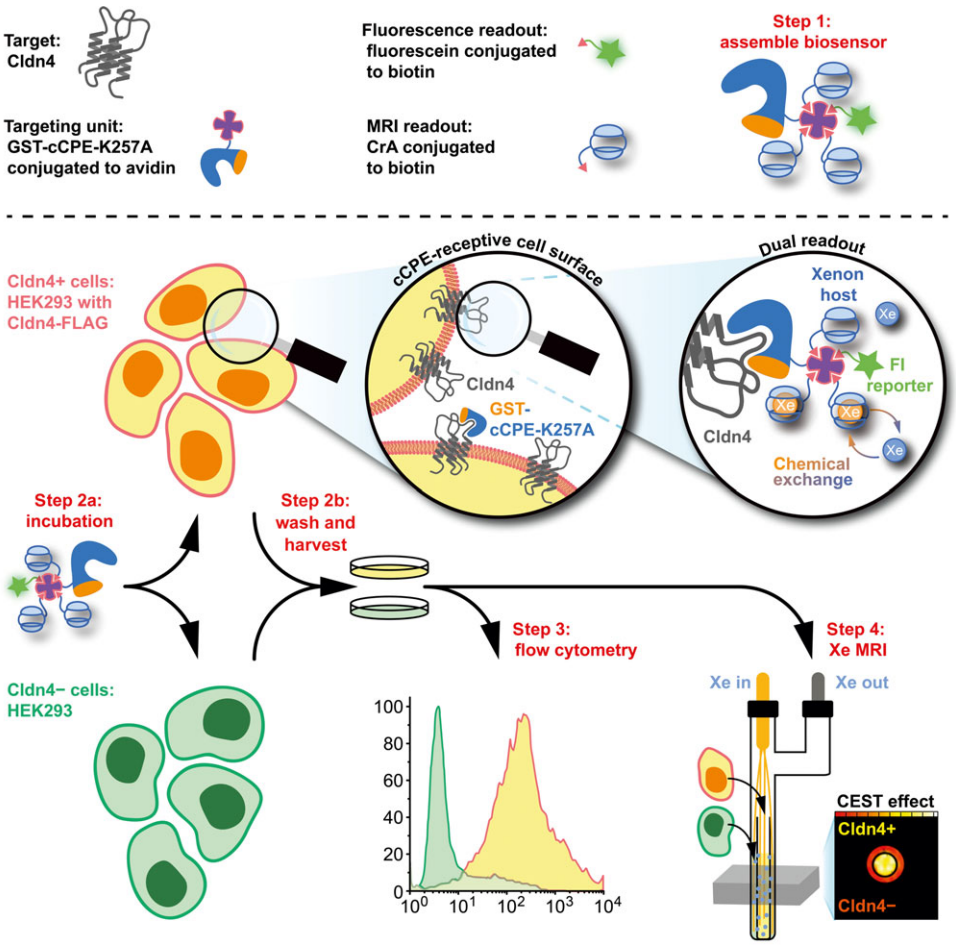

Figure 2. Experimental design. The Cldn4 biosensor comprises an avidin-conjugated cCPE targeting module and a set of biotin-conjugated readout modules for dual functionality (MRI/fluorescence) to selectively label Cldn4-expressing cells. Step 1: for the complete biosensor preparation, the targeting modules and readout modules were mixed. Step 2a: cells were incubated with the biosensor. Step 2b: cells were washed to remove any unbound biosensor and harvested. The Cldn4^{+} cells were then decorated on their surface with the dual readout sensor. In particular, the xenon (Xe) hosts reversibly bound Xe atoms (orange) to affect the MR signal of free Xe (blue) through chemical exchange. Step 3: binding to cells; biosensor specificity (and cellular localization) could be evaluated via the fluorescence readout module. Step 4: the cell suspensions were placed into separate compartments within a double phantom for ^{129}Xe MRI: nontransfected HEK cells in the outer compartment, Cldn4-FLAG-transfected cells in the inner one. Hyperpolarized xenon was bubbled through the samples for MRI detection. Illustrative xenon MRI shows a cross-section of the NMR double phantom. The intensity of CEST effect in the inner and outer compartment is used to judge specificity of biosensor contrast.

xenografts with overexpressed claudins.[13] In a study by Cocco *et al.*, cCPE labeled with either FITC or a near-infrared fluorescent tag was injected into mice at dosages of 10 and 25 μg, respectively, and later detected *in vivo* by fluorescence stereo microscopy.[51] In that study, detection of cCPE binding to claudins by the optical imaging system was suggested as an intraoperative tool. However, for noninvasive diagnostic detection, fluorescence-based imaging is limited by penetration depth and autofluorescence. As an alternative, ^{111}In radiolabeled cCPE and single-photon emission computed tomography were used to detect Cldn4^{+} MDA-MB-468 xenograft and other tumors in mice.[52] Here, the radiation exposure has to be considered as a drawback.

In our current study, we tried to overcome the limitations of fluorescence- or radiolabel-based

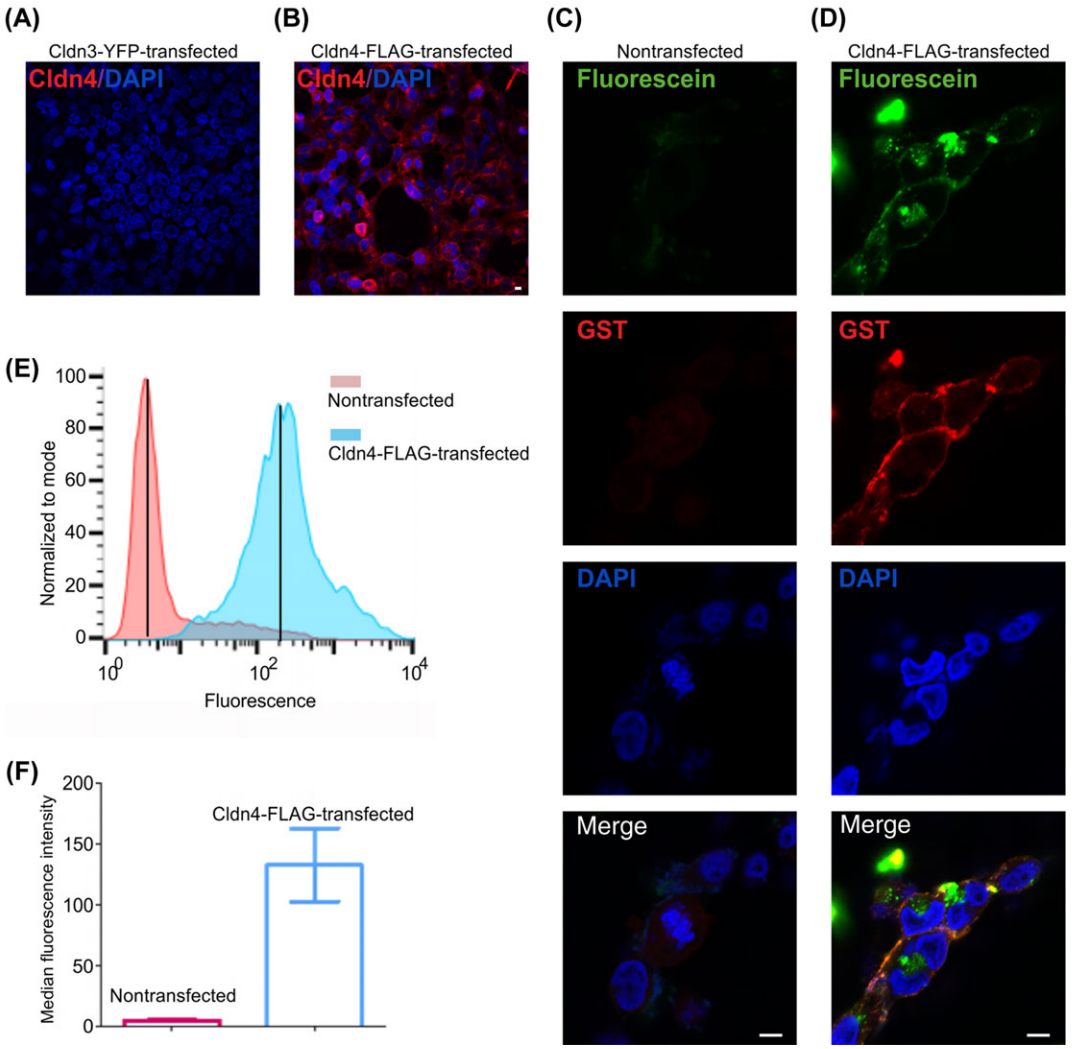

Figure 3. Binding of labeled GST–cCPE-K257A specifically to Cldn4–FLAG in HEK cells. (A–D) Confocal microscopy demonstrating expression, localization, and biosensor binding of Cldn4 in HEK cells. In contrast to a Cldn3–YFP–expressing (HEK control cell line, A) line, the Cldn4–FLAG HEK line showed anti-Cldn4 immunoreactivity in the periphery of the cells (B). (C) After incubation with the Cldn4 biosensor, nontransfected HEK control cells showed neither fluorescein fluorescence (green) nor anti-GST immunoreactive signals (red). (D) For Cldn4–FLAG–expressing HEK cells, fluorescein fluorescence (green) was detected on the cell surface and in intracellular compartments. Anti-GST immunoreactive signals (red) were detected on the cell surface only, owing to omission of plasma membrane permeabilization. Cells were either fixed with methanol (A, B) or with 3.7% PFA (C, D) without membrane permeabilization and stained with DAPI (blue), and (A, B) mouse-anti Cldn4 antibodies (red) or mouse-anti-GST antibodies. Bar, 5 μm. (E, F) Evaluation of biosensor binding to cells by flow cytometry. The total/absolute fluorescence of the cells was measured by flow cytometry. Cldn4–FLAG–transfected HEK cells showed a much higher fluorescence intensity than nontransfected HEK cells. (E) This signal emitted by the fluorescein–biotin readout module demonstrated that the biosensor binds specifically to Cldn4-transfected HEK cells. Representative experiment; median is shown as black line. (D) Quantification of fluorescence intensity of three independent experiments. Mean of individual medians and SEM.

imaging by employing highly sensitive xenon Hyper-CEST biosensors. With an effectively unlimited penetration depth, an MRI biosensor targeted to claudins has the potential to be a valuable diagnostic tool. However, one critical aspect of any such biosensor is its sensitivity. Conventional MRI contrast agents, such as Gd chelates, function by increasing the relaxation rate of water protons in

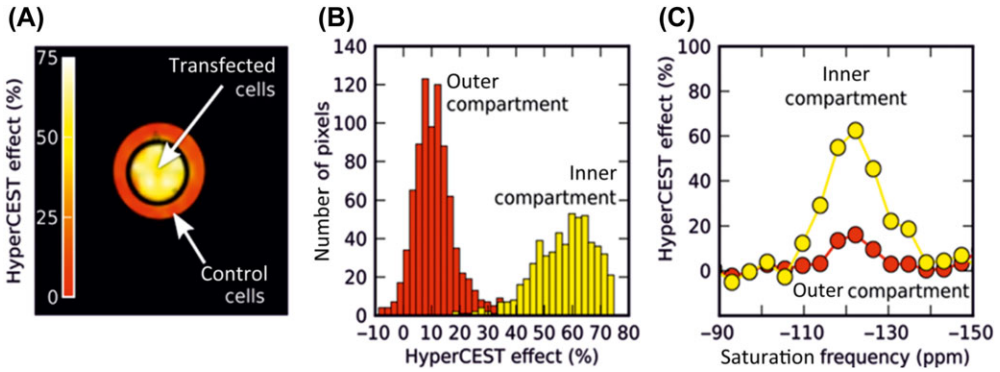

Figure 4. Claudin-4 targeted xenon Hyper-CEST imaging. (A) Xenon Hyper-CEST imaging correctly localizes the cells expressing Cldn4 in the inner compartment of the phantom as demonstrated by the high Hyper-CEST effect. The image displays the Hyper-CEST image (false color) overlaid with a high-resolution ^{1}H MRI scan for reference (black and white in the background to define the geometry outline of the compartments for orientation). The xenon Hyper-CEST images were acquired using a 30-μT, 20-s saturation pulse with one image for each saturation frequency and 10 averages for each on- and off-resonance image. (B) The histogram of the Hyper-CEST effect clearly shows the ∼6-fold higher Hyper-CEST in the target compartment. (C) By segmenting the images into two regions of interest (the inner and outer compartments) and saturating at different frequencies, we can construct a localized Hyper-CEST spectrum for each of the compartments. The strong response around –120 ppm (referenced to the resonance frequency of xenon free in solution) is a characteristic of xenon bound to the host Cr-A in a lipidic/cellular environment.[16,39]

their vicinity. To generate sufficient contrast in an image, they typically require local concentrations in the very high micromolar to millimolar range. As many of the most interesting targets are below this concentration, this has seriously limited the use of targeted MRI reporters.

The sensitivity enhancement of Hyper-CEST pays off especially for cell surface targets where the contrast agent cannot be accumulated by internalization through a relatively small number of transporters. Aiming for sialic acid residues as part of exposed glycans, coupling of an MRI relaxivity contrast agent to such a cellular surface target has been demonstrated in an elegant way.[53] But the study made clear that, for the investigated cell type, this is a highly expressed target with about 10^9 copies per cell. This number matches general estimates when assuming that the detection limit of relaxivity agents is considered to be in the micromolar range.[15,54,55] MRI validation of novel agents in cell suspensions is typically done at densities of 10^6–10^7 cells/mL. A detection limit of 10 μM agent concentration would require $\sim 10^9$ copies of a cell surface target per cell when using 5×10^6 cells/mL. Cldn4 expression can be assumed to be significantly lower for the cells used in our study and would therefore be inaccessible with the relaxivity approach.

To develop a claudin-targeted MRI biosensor that can take advantage of the high sensitivity of xenon biosensor, we built upon our modular xenon biosensor platform.[42] This design separates the biosensor into two functional units, a "readout module" and a "targeting module." These two modules are connected by the high-affinity binding partners avidin and biotin. The modular nature of this design allowed us to efficiently reuse our previous readout modules, biotin–CrA (for readout via xenon MRI) and biotin–FITC (for readout via fluorescence). This significantly reduced the time and monetary investment in design and construction of new chemical constructs.

The sialic acid study also showed that incubation concentrations can easily be in the high micromolar range (600 μM in that case) to ensure sufficient labeling when binding is not based on a highly specific recognition motif. Relying on the cCPE–Cldn binding concept was therefore also motivated by the idea to decrease the incubation concentration significantly. Using 18 μg/mL corresponds to only 160 nM biosensor concentration. While the mass of the assembled biosensor (113 kDa) is admittedly larger than those of typical low-molecular-weight Gd contrast agents, this can still be considered a minimally invasive cell labeling.

In designing the targeting module, we ensured that conjugation of avidin to lysines in cCPE did not reduce binding affinity to claudins. In particular, K257—which is very close to the claudin-binding pocket of cCPE (Fig. 1)—was substituted against alanine, since we showed previously that GST–cCPE-K257A with or without a fluorescent label binds efficiently to Clnd3- or Cldn4-expressing cells.[44,56] Additionally, as avidin contains four binding sites for biotin, and there is the potential to conjugate multiple avidins on each GST–cCPE-K257A unit, this gives us an additional amplification factor. The resulting biosensor GST–cCPE–avidin–biotin–FITC and –biotin–CrA showed a labeling easily detectable by both fluorescence and hyperpolarized xenon MRI.

Though, in these preliminary experiments, we used a rather thick slice of 2 cm; there are no inherent limitations on the slice thickness with this method apart from the signal to noise ratio (SNR), a practical limit on all MRIs. Using this setup, we could achieve the same SNR with a 2-mm slice by sacrificing in-plane resolution (2 mm × 2 mm × 2 mm voxels would give us slightly better SNR). Alternatively, to maintain the in-plane resolution, other techniques could be used to improve the SNR. In these experiments, we used a gas mix of 5% xenon at a total pressure of 4.5 bar. As is typically done for *in vivo* hyperpolarized xenon experiments, by freezing out the xenon using a cold trap, it is possible to deliver pure xenon at 1 bar of total pressure, potentially improving the SNR by a factor of 4.4. Using isotope-enriched xenon can further increase the NMR active spin-1/2 nuclei ^{129}Xe by an additional factor of 3. Furthermore, we currently achieve a polarization of approximately 25%. Newer polarizer designs can achieve polarization approaching 100%,[22] which could further improve the SNR by an additional factor of 4. In fact, because of the more challenging conditions, some combination of these enhancements would also likely be required for future *in vivo* experiments.

Though the transition to *in vivo* experiments is likely challenging, there is also reason to assume no fundamental barriers. Even with the shorter T_1 *in vivo*, recent experiments have shown that not only is hyperpolarized xenon able to be imaged in the rodent brain,[24,25] but also in the human brain.[26] In addition, as xenon biosensors are based not on relaxation but chemical shift, they would have an insignificant effect on *in vivo* T_1 relaxation rates. Additionally, recent pharmacokinetic modeling of Hyper-CEST imaging *in vivo*, using realistic assumptions about xenon hyperpolarization, delivery, T_1, and saturation, demonstrates that sufficient contrast should be achievable in the rat brain.[30]

When envisaging possible future *in vivo* applications, some modification of this biosensor should also be considered. In particular, it has been shown that streptavidin has a higher retention time in the bloodstream and is cleared predominantly via the renal system rather than hepatic clearance.[57] Additionally, alternative biotin derivatives have been shown to be more biologically stable,[58] and to reduce the effect of endogenous biotin binding to the targeting module, biotin-deficient diets should be used in mouse models.[59] For *in vivo* applications, the immunogenicity of the avidin/streptavidin–biotin system has to be considered, though this has not prevented the use of avidin-based pretargeting in *in vivo* studies.[60] In mouse models, high anti-avidin antibody titers corresponding to those found in avidin-treated oncology patients did not affect the safety and efficacy of avidin–biotin treatment, thus encouraging its applications.[61] However, in cases where such immunogenicity is problematic, alternative coupling strategies should be considered, such as directly coupling one or more CrA molecules to the cCPE peptide.

Concerning the claudin-targeting module, cCPE variants with modified claudin-binding properties could be used. Structure-guided mutagenesis led to cCPE variants preferentially binding to either Cldn3 (cCPEL223A/D225A/R227A) or Cldn4 (cCPEL254A/S256A/I258A/D284A)[44] or binding to Cldn5 (cCPEY306W/S313H).[56] In addition, phage display yielded a broad specific claudin binder (cCPES305P/S307R/S313H).[62] The latter also interacts with Cldn1, a claudin that was recently targeted by fluorophore-labeled Cldn1-mimetic binding peptide for endoscopic detection of Cldn1 overexpression in mice, a hallmark of colon cancer.[63] However, the signal-to-noise ratio was quite low, which might be improved by use of a Cldn1-binding cCPE-variant xenon biosensor.

In addition to the potential diagnostic value of cCPE, treatment with cytotoxic full-length CPE reduced tumor growth in mouse models.[64,65] This underlines the efficiency of claudin targeting using the claudin-binding domain of CPE.

Here, we developed, on a base of cCPE, a new Cldn3/4–sensitive xenon Hyper-CEST biosensor for detection of overexpressed claudins in tumors. Not only does this demonstrate the flexibility of our xenon biosensor platform by extending it beyond antibody targeting, but it also presents one possible pathway for translating the detection of Cldn3/4 to an MRI diagnostic tool. This biosensor would make an attractive candidate for the first *in vivo* xenon biosensor experiments.

Acknowledgments

We thank Dr. Susanne Milatz (Institute of Physiology, Kiel, Germany) for kindly providing the plasmid pCMV10/huCldn4. The experiments were performed by Anna Piontek, Christopher Witte, Honor Rose, Miriam Eichner, and Jonas Protze. The structural bioinformatics and modeling were performed by Jonas Protze, Jörg Piontek, and Gerd Krause. Anna Piontek, Christopher Witte, Jörg Piontek, Jonas Protze, Gerd Krause, and Leif Schröder wrote the paper. Jörg Piontek, Gerd Krause, and Leif Schröder designed and managed the study. This work was supported by the European Research Council (ERC) under the European Community's Seventh Framework Programme (FP7/2007-2013)/ERC Grant Agreement 242710, the Leibniz Association (Wissenschaftsgemeinschaft Gottfried Wilhelm Leibniz e.V.; Grant SAW-2011-FMP-2), the Federal Ministry of Education and Research (BMBF) Grant 13EZ1010B, and the Human Frontier Science Program (C.W.), Deutsche Forschungsgemeinschaft grant KR1273/8-1 (G.K.), Wilhelm Sander Stiftung, Munich, Germany 215.112.1 (G.K.), and the Sonnenfed Stiftung, Berlin, Germany (M.E.).

Supporting Information

Additional supporting information may be found in the online version of this article.

Figure S1. Post processing of xenon images. Raw xenon images after off- and on-resonant saturation.

Figure S2. Segmentation of Hyper-CEST images. High resolution proton images (upper left) were used to automatically segment the xenon images.

Competing interests

The authors declare no competing interests.

References

1. Günzel, D. & M. Fromm. 2012. Claudins and other tight junction proteins. *Compr. Physiol.* **2:** 1819–1852.
2. Kwon, M.J. 2013. Emerging roles of claudins in human cancer. *Int. J. Mol. Sci.* **14:** 18148–18180.
3. Osanai, M., A. Takasawa, M. Murata, *et al.* 2017. Claudins in cancer: bench to bedside. *Pflugers Arch.* **469:** 55–67.
4. de Oliveira, S.S., I.M. de Oliveira, W. De Souza, *et al.* 2005. Claudins upregulation in human colorectal cancer. *FEBS Lett.* **579:** 6179–6185.
5. Boireau, S., M. Buchert, M.S. Samuel, *et al.* 2007. DNA-methylation-dependent alterations of claudin-4 expression in human bladder carcinoma. *Carcinogenesis* **28:** 246–
258.
6. Lioni, M., P. Brafford, C. Andl, *et al.* 2007. Dysregulation of claudin-7 leads to loss of E-cadherin expression and the increased invasion of esophageal squamous cell carcinoma cells. *Am. J. Pathol.* **170:** 709–721.
7. Eichner, M., J. Protze, A. Piontek, *et al.* 2017. Targeting and alteration of tight junctions by bacteria and their virulence factors such as *Clostridium perfringens* enterotoxin. *Pflugers Arch.* **469:** 77–90.
8. Veshnyakova, A., J. Protze, J. Rossa, *et al.* 2010. On the interaction of *Clostridium perfringens* enterotoxin with claudins. *Toxins* **2:** 1336–1356.
9. Kokai-Kun, J.F. & B.A. McClane. 1997. Deletion analysis of the *Clostridium perfringens* enterotoxin. *Infect. Immun.* **65:** 1014–1022.
10. Suzuki, H., M. Kondoh, X. Li, *et al.* 2011. A toxicological evaluation of a claudin modulator, the C-terminal fragment of *Clostridium perfringens* enterotoxin, in mice. *Pharmazie* **66:** 543–546.
11. McClane, B.A. 2001. The complex interactions between *Clostridium perfringens* enterotoxin and epithelial tight junctions. *Toxicon* **39:** 1781–1791.
12. Takahashi, A., E. Komiya, H. Kakutani, *et al.* 2008. Domain mapping of a claudin-4 modulator, the C-terminal region of C-terminal fragment of *Clostridium perfringens* enterotoxin, by site-directed mutagenesis. *Biochem. Pharmacol.* **75:** 1639–1648.
13. Neesse, A., A. Hahnenkamp, H. Griesmann, *et al.* 2013. Claudin-4-targeted optical imaging detects pancreatic cancer and its precursor lesions. *Gut* **62:** 1034–1043.
14. English, D.P. & A.D. Santin. 2013. Claudins overexpression in ovarian cancer: potential targets for *Clostridium perfringens* enterotoxin (CPE) based diagnosis and therapy. *Int. J. Mol. Sci.* **14:** 10412–10437.
15. Caravan, P. 2009. Protein-targeted gadolinium-based magnetic resonance imaging (MRI) contrast agents: design and mechanism of action. *Acc. Chem. Res.* **42:** 851–862.
16. Klippel, S., J. Döpfert, J. Jayapaul, *et al.* 2014. Cell tracking with caged xenon: using cryptophanes as MRI reporters upon cellular internalization. *Angew. Chem. Int. Ed. Engl.* **53:** 493–496.
17. Kunth, M., C. Witte, A. Hennig, *et al.* 2015. Identification, classification, and signal amplification capabilities of high-turnover gas binding hosts in ultra-sensitive NMR. *Chem. Sci.* **6:** 6069–6075.

18. Shapiro, M.G., R.M. Ramirez, L.J. Sperling, *et al.* 2014. Genetically encoded reporters for hyperpolarized xenon magnetic resonance imaging. *Nat. Chem.* **6:** 629–634.
19. Schroder, L. 2013. Xenon for NMR biosensing—inert but alert. *Phys. Med.* **29:** 3–16.
20. Walker, T.G. & W. Happer. 1997. Spin-exchange optical pumping of noble-gas nuclei. *Rev. Mod. Phys.* **69:** 629–642.
21. Witte, C., M. Kunth, F. Rossella, *et al.* 2014. Observing and preventing rubidium runaway in a direct-infusion xenon-spin hyperpolarizer optimized for high-resolution hyper-CEST (chemical exchange saturation transfer using hyperpolarized nuclei) NMR. *J. Chem. Phys.* **140:** 084203.
22. Nikolaou, P., A.M. Coffey, L.L. Walkup, *et al.* 2013. Near-unity nuclear polarization with an open-source ^{129}Xe hyperpolarizer for NMR and MRI. *Proc. Natl. Acad. Sci. U.S.A.* **110:** 14150–14155.
23. Mugler, J.P., 3rd & T.A. Altes. 2013. Hyperpolarized ^{129}Xe MRI of the human lung. *J. Magn. Reson. Imaging* **37:** 313–331.
24. Zhou, X., M.L. Mazzanti, J.J. Chen, *et al.* 2008. Reinvestigating hyperpolarized (129)Xe longitudinal relaxation time in the rat brain with noise considerations. *NMR Biomed.* **21:** 217–225.
25. Duhamel, G., P. Choquet, E. Grillon, *et al.* 2001. Xenon-129 MR imaging and spectroscopy of rat brain using arterial delivery of hyperpolarized xenon in a lipid emulsion. *Magn. Reson. Med.* **46:** 208–212.
26. Rao, M., N.J. Stewart, G. Norquay, *et al.* 2016. High resolution spectroscopy and chemical shift imaging of hyperpolarized ^{129}Xe dissolved in the human brain *in vivo* at 1.5 tesla. *Magn. Reson. Med.* **75:** 2227–2234.
27. Spence, M.M., E.J. Ruiz, S.M. Rubin, *et al.* 2004. Development of a functionalized xenon biosensor. *J. Am. Chem. Soc.* **126:** 15287–15294.
28. Wang, Y. & I.J. Dmochowski. 2015. Cucurbit[6]uril is an ultrasensitive (129)Xe NMR contrast agent. *Chem. Commun.* **51:** 8982–8985.
29. Stevens, T.K., R.M. Ramirez & A. Pines. 2013. Nanoemulsion contrast agents with sub-picomolar sensitivity for xenon NMR. *J. Am. Chem. Soc.* **135:** 9576–9579.
30. Shapiro, M.G., R.M. Ramirez, L.J. Sperling, *et al.* 2014. Genetically encoded reporters for hyperpolarized xenon magnetic resonance imaging. *Nat. Chem.* **6:** 629–634.
31. Randtke, E.A., J.C. Granados, C.M. Howison, *et al.* 2016. Multislice CEST MRI improves the spatial assessment of tumor pH. *Magn. Reson. Med.* https://doi.org/10.1002/mrm.26348.
32. Moon, B.F., K.M. Jones, L.Q. Chen, *et al.* 2015. A comparison of iopromide and iopamidol, two acidoCEST MRI contrast media that measure tumor extracellular pH. *Contrast Media Mol. Imaging* **10:** 446–455.
33. Longo, D.L., P.Z. Sun, L. Consolino, *et al.* 2014. A general MRI-CEST ratiometric approach for pH Imaging: demonstration of *in vivo* pH mapping with iobitridol. *J. Am. Chem. Soc.* **136:** 14333–14336.
34. Sinharay, S., E.A. Randtke, K.M. Jones, *et al.* 2016. Noninvasive detection of enzyme activity in tumor models of human ovarian cancer using catalyCEST MRI. *Magn. Reson. Med.* **77:** 2005–2014.
35. Sinharay, S., G. Fernandez-Cuervo, J.P. Acfalle, *et al.* 2016. Detection of sulfatase enzyme activity with a catalyCEST MRI contrast agent. *Chemistry* **22:** 6491–6495.
36. Aime, S., D. Delli Castelli & E. Terreno. 2002. Novel pH-reporter MRI contrast agents. *Angew. Chem. Int. Ed. Engl.* **41:** 4334–4336.
37. Aime, S., D. Delli Castelli & E. Terreno. 2005. Highly sensitive MRI chemical exchange saturation transfer agents using liposomes. *Angew. Chem. Int. Ed.* **44:** 5513–5515.
38. Ferrauto, G., D. Delli Castelli, E. Di Gregorio, *et al.* 2014. Lanthanide-loaded erythrocytes as highly sensitive chemical exchange saturation transfer MRI contrast agents. *J. Am. Chem. Soc.* **136:** 638–641.
39. Ferrauto, G., E. Di Gregorio, S. Baroni, *et al.* 2014. Frequency-encoded MRI-CEST agents based on paramagnetic liposomes/RBC aggregates. *Nano Lett.* **14:** 6857–6862.
40. Schroder, L., T.J. Lowery, C. Hilty, *et al.* 2006. Molecular imaging using a targeted magnetic resonance hyperpolarized biosensor. *Science* **314:** 446–449.
41. Hingorani, D.V., A.S. Bernstein & M.D. Pagel. 2015. A review of responsive MRI contrast agents: 2005–2014. *Contrast Media Mol. Imaging* **10:** 245–265.
42. Rose, H.M., C. Witte, F. Rossella, *et al.* 2014. Development of an antibody-based, modular biosensor for ^{129}Xe NMR molecular imaging of cells at nanomolar concentrations. *Proc. Natl. Acad. Sci. U.S.A.* **111:** 11697–11702.
43. Winkler, L., C. Gehring, A. Wenzel, *et al.* 2009. Molecular determinants of the interaction between *Clostridium perfringens* enterotoxin fragments and claudin-3. *J. Biol. Chem.* **284:** 18863–18872.
44. Veshnyakova, A., J. Piontek, J. Protze, *et al.* 2012. Mechanism of *Clostridium perfringens* enterotoxin interaction with claudin-3/-4 protein suggests structural modifications of the toxin to target specific claudins. *J. Biol. Chem.* **287:** 1698–1708.
45. Piontek, J., S. Fritzsche, J. Cording, *et al.* 2011. Elucidating the principles of the molecular organization of heteropolymeric tight junction strands. *Cell. Mol. Life Sci.* **68:** 3903–3918.
46. Witte, C., M. Kunth, J. Döpfert, *et al.* 2012. Hyperpolarized xenon for NMR and MRI applications. *J. Vis. Exp.* https://doi.org/10.3791/4268.
47. Hennig, J., A. Nauerth & H. Friedburg. 1986. RARE imaging: a fast imaging method for clinical MR. *Magn. Reson. Med.* **3:** 823–833.
48. Van Itallie, C.M., L. Betts, J.G. Smedley, *et al.* 2008. Structure of the claudin-binding domain of *Clostridium perfringens* enterotoxin. *J. Biol. Chem.* **283:** 268–274.
49. Siegel, R., J. Ma, Z. Zou, *et al.* 2014. Cancer statistics, 2014. *CA Cancer J. Clin.* **64:** 9–29.
50. Coleman, R.L., B.J. Monk, A.K. Sood, *et al.* 2013. Latest research and treatment of advanced-stage epithelial ovarian cancer. *Nat. Rev. Clin. Oncol.* **10:** 211–224.
51. Cocco, E., E.M. Shapiro, S. Gasparrini, *et al.* 2015. *Clostridium perfringens* enterotoxin C-terminal domain labeled to fluorescent dyes for *in vivo* visualization of micrometastatic chemotherapy-resistant ovarian cancer. *Int. J. Cancer* **137:** 2618–2629.

52. Mosley, M., J. Knight, A. Neesse, *et al.* 2015. Claudin-4 SPECT imaging allows detection of Aplastic lesions in a mouse model of breast cancer. *J. Nucl. Med.* **56:** 745–751.
53. Geninatti, C.S., D. Alberti, I. Szabo, *et al.* 2013. MRI visualization of melanoma cells by targeting overexpressed sialic acid with a Gd(III)-dota-en-pba imaging reporter. *Angew. Chem. Int. Ed.* **52:** 1161–1164.
54. Ahrens, E.T., U. Rothbacher, R.E. Jacobs, *et al.* 1998. A model for MRI contrast enhancement using T1 agents. *Proc. Natl. Acad. Sci. U.S.A.* **95:** 8443–8448.
55. Mills, P.H. & E.T. Ahrens. 2007. Theoretical MRI contrast model for exogenous T2 agents. *Magn. Reson. Med.* **57:** 442–447.
56. Protze, J., M. Eichner, A. Piontek, *et al.* 2015. Directed structural modification of *Clostridium perfringens* enterotoxin to enhance binding to claudin-5. *Cell. Mol. Life Sci.* **72:** 1417–1432.
57. Sakahara, H. & T. Saga. 1999. Avidin–biotin system for delivery of diagnostic agents. *Adv. Drug Deliv. Rev.* **37:** 89–101.
58. Foulon, C.F., K.L. Alston & M.R. Zalutsky. 1998. Astatine-211-labeled biotin conjugates resistant to biotinidase for use in pretargeted radioimmunotherapy. *Nucl. Med. Biol.* **25:** 81–88.
59. Hamblett, K.J., B.B. Kegley, D.K. Hamlin, *et al.* 2002. A streptavidin–biotin binding system that minimizes blocking by endogenous biotin. *Bioconjug. Chem.* **13:** 588–598.
60. Patra, M., K. Zarschler, H.J. Pietzsch, *et al.* 2016. New insights into the pretargeting approach to image and treat tumours. *Chem. Soc. Rev.* **45:** 6415–6431.
61. Petronzelli, F., A. Pelliccia, A.M. Anastasi, *et al.* 2010. Therapeutic use of avidin is not hampered by antiavidin antibodies in humans. *Cancer Biother. Radiopharm.* **25:** 563–570.
62. Takahashi, A., Y. Saito, M. Kondoh, *et al.* 2012. Creation and biochemical analysis of a broad-specific claudin binder. *Biomaterials* **33:** 3464–3474.
63. Rabinsky, E.F., B.P. Joshi, A. Pant, *et al.* 2016. Overexpressed claudin-1 can be visualized endoscopically in colonic adenomas *in vivo*. *Cell. Mol. Gastroenterol. Hepatol.* **2:** 222–237.
64. Kominsky, S.L., B. Tyler, J. Sosnowski, *et al.* 2007. *Clostridium perfringens* enterotoxin as a novel-targeted therapeutic for brain metastasis. *Cancer Res.* **67:** 7977–7982.
65. Walther, W., S. Petkov, O.N. Kuvardina, *et al.* 2012. Novel *Clostridium perfringens* enterotoxin suicide gene therapy for selective treatment of claudin-3- and -4-overexpressing tumors. *Gene Ther.* **19:** 494–503.
66. Shinoda, T., N. Shinya, K. Ito, *et al.* 2016. Structural basis for disruption of claudin assembly in tight junctions by an enterotoxin. *Sci. Rep.* **6:** 33632.